HHS Public Access

Author manuscript

Mol Imaging Biol. Author manuscript; available in PMC 2016 October 01.

Published in final edited form as:

Mol Imaging Biol. 2016 October ; 18(5): 677–685. doi:10.1007/s11307-016-0932-2.

Detection of Lymph Node Metastases with SERRS Nanoparticles

Massimiliano Spaliviero[1,2,*], **Stefan Harmsen**[1,*], **Ruimin Huang**[1,*], **Matthew A. Wall**[1,3,4], **Chrysafis Andreou**[1], **James A. Eastham**[2], **Karim A. Touijer**[2], **Peter T. Scardino**[2], and **Moritz F. Kircher**[1,5,6,#]

[1]Department of Radiology, Memorial Sloan Kettering Cancer Center, New York, NY 10065, USA

[2]Urology Service, Department of Surgery, Sidney Kimmel Center for Prostate and Urologic Cancers, Memorial Sloan Kettering Cancer Center, New York, NY 10065, USA

[3]Department of Chemistry, Hunter College of the City University of New York, New York, NY 10065, USA

[4]Department of Chemistry, The Graduate Center of the City University of New York, New York, NY 10065, USA

[5]Center for Molecular Imaging and Nanotechnology, Memorial Sloan Kettering Cancer Center, New York, NY 10065, USA

[6]Department of Radiology, Weill Cornell Medical College, New York, NY 10065, USA

Abstract

Purpose—The accurate detection of lymph node metastases in prostate cancer patients is important to direct treatment decisions. Our goal was to develop an intra-operative imaging approach to distinguish normal from metastasized lymph nodes. We therefore developed and tested gold-silica surface-enhanced resonance Raman spectroscopy (SERRS) nanoparticles that demonstrate high uptake within normal lymphatic tissue, and negligible uptake in areas of metastatic replacement.

Procedures—We evaluated the ability of SERRS nanoparticles to delineate lymph node metastases in an orthotopic prostate cancer mouse model using PC-3 cells transduced with mCherry fluorescent protein. Tumor bearing mice ($n = 6$) and non-tumor bearing control animals ($n = 4$) were injected intravenously with 30 fmol/g SERRS nanoparticles. After 16–18 hours, the retroperitoneal lymph nodes were scanned *in situ* and *ex vivo* with a Raman imaging system and a

[#]To whom correspondence should be addressed. kircherm@mskcc.org.
[*]These authors contributed equally to this work

Author contributions:
The project was conceptualized by M.F.K. with the goal to develop a Raman imaging approach for detection of lymph node metastases. The project was supervised by M.F.K. The study was designed by M.F.K., M.S., S.H., and R.H. Data acquisition was performed by M.S., S.H, R.H., and M.S., S.H, R.H., C.A., M.A.W., J.A.E., K.A.T., P.T.S., and M.F.K. participated in the design and/or interpretation of the reported experiments or results. C.A. performed data analysis. M.S., S.H, R.H., and M.F.K. wrote the manuscript, which was reviewed and approved by all authors.

Conflicts of interest
S.H., M.A.W. and M.F.K. are inventors on pending patents regarding the SERRS nanoparticle design and synthesis procedures. M.F.K. is the inventor of an additional pending patent regarding a wide-field Raman scanner and is a co-founder of RIO Imaging, Inc.

hand-held Raman scanner and data corroborated with fluorescence imaging for mCherry protein expression and histology.

Results—The SERRS nanoparticles demonstrated avid homing to normal lymph nodes, but not to metastasized lymph nodes. In cases where lymph nodes were partially infiltrated by tumor cells, the SERRS signal correctly identified, with sub-millimeter precision, healthy from metastasized components within the same lymph node.

Conclusions—This study serves as a first proof-of-principle that SERRS nanoparticles enable high precision and rapid intraoperative discrimination between normal and metastasized lymph nodes.

Keywords

Surface-enhanced resonance Raman scattering; Raman imaging; prostate cancer; lymph node metastasis; intraoperative imaging

INTRODUCTION

Prostate cancer (PCa), the most commonly diagnosed and second most lethal cancer in men in the US, accounts for 26% of incident cancer cases and 9% of cancer deaths annually [1]. Radical prostatectomy (RP) is the most widely used treatment for localized PCa and selected patients with high-risk PCa [2].

Pelvic lymph node dissection (PLND) during RP provides accurate and critically important staging information regarding prostate cancer extent, since metastatic pelvic lymph nodes are found in 3% to 26% of patients with no radiographic evidence of regional spread of the disease [3–6]. Recent series have also shown that PLND may have a therapeutic benefit as select patients with favorable pathologic features and limited nodal metastases appeared to be cured by the combination of RP and PLND alone [3, 7–8]. Since its introduction, widespread prostate-specific antigen (PSA) testing resulted in PCa stage migration and the decline of the risk of metastatic nodes at presentation. This, in combination with the availability of nomograms [9] assessing the individual's risk for node positivity, contributed to the decline of the proportion of patients who receive PLND as well as the extent and yield of PLND [10–12]. However, the accurate detection of lymph node metastases remains particularly important for staging purposes [13] since most nomograms may underestimate the true risk of nodal metastasis [14–15], and for the therapeutic benefit of PLND.

Historically, several imaging approaches have been used to map lymphatic drainage of the prostate, and PCa in particular. However, no reliable imaging modality to detect lymph node metastases is currently available [13]. Primarily using size criteria, both computed tomography (CT) and magnetic resonance imaging (MRI) typically lack sensitivity for the detection of metastases of less than one centimeter in size, which are the most common type of metastases occurring in contemporary series [5, 16]. Sentinel node lymphoscintigraphy after injection of the prostate with radioactive or fluorescent imaging agents detected with single-photon emission CT/CT (SPECT/CT), near-infrared fluorescence guidance, or a hybrid radiocolloid, have low cancer specificity [17–18]. Superparamagnetic iron oxide nanoparticles (SPIONs) of different sizes and compositions were tested as MRI

lymphography contrast agents and showed promising preclinical and clinical results [19–22]; however, they were not granted Food and Drug Administration approval for clinical use in the United States. In addition, while SPION-enhanced MRI could provide a preoperative roadmap, it is not suitable for intraoperative imaging. Intraoperative MRI scanners are only available at a few selected medical centers due to their high cost and large footprint, and the image acquisition times required for high resolution imaging prevent real-time decision making in the operating room.

Intraoperative optical imaging has attracted much attention as it has the potential to enable rapid intraoperative tumor visualization, and with devices that are financially affordable, have small footprints, and can be customized to fit well into the surgical workflow. Among the different principles of optical imaging, surface-enhanced Raman scattering (SERS) imaging is one of the most recently developed techniques. It has several fundamental advantages over fluorescence imaging methods, which include higher sensitivity, higher signal specificity, absence of photobleaching, and multiplexing capabilities [23]. It was previously shown that non-resonant SERS nanoparticles accurately delineate high-grade gliomas and allow intraoperative SERS-guided brain tumor resection in an orthotopic mouse model [24]. To provide maneuverability, the intraoperative use of a hand-held Raman scanner for SERS-guided brain tumor resection was evaluated and shown to accurately detect residual tumor tissue after supposed radical resection [25].

To further improve the detectability and general application of Raman imaging for (intraoperative) tumor delineation, we recently developed a new generation of SERRS nanoparticles that are 400-fold brighter and were shown to detect the primary prostate cancer with microscopic precision in the transgenic Hi-Myc mouse model [26]. However, the latter model generally does not produce lymph node metastases. In this proof-of-concept study we therefore aimed at testing SERRS nanoparticles in an orthotopic prostate cancer mouse model which is known to produce lymph node metastases, and determine whether these can be detected with Raman spectroscopy and spectroscopic imaging as illustrated in Fig. 1a.

MATERIALS AND METHODS

Chemicals

All chemicals were obtained from Sigma Aldrich (St. Louis, MO) and used as received. PC-3 cells were obtained from ATCC (Manassas, VA; CRL-1435).

SERRS nanoparticle synthesis

To 1.0 L of a boiling aqueous solution of 0.25 mM gold chloride 7.5 mL 1% (w/v) sodium citrate tribasic dihydrate was added. The as-synthesized 60-nm gold nanoparticles were collected by centrifugation and dialyzed (Slide-a-lyzer G2; MWCO: 3.5 kDa; Thermo Fisher Scientific, Inc. Waltham, MA). The dialyzed 60-nm gold nanoparticles were encapsulated in resonant Raman reporter (IR780 perchlorate)-embedded silica via a modified Stöber procedure. To 43 mL isopropanol, 650 μL 28% (v/v) ammonium hydroxide, 1.3 mL tetraethyl orthosilicate, a 4.5 mL 2.0 nM aqueous dispersion of dialyzed 60-nm gold

nanoparticles, and 100 μL 20 mM IR780 perchlorate in *N,N*-dimethylformamide were added and allowed to react for 15 minutes. The as-synthesized SERRS nanoparticles were collected by centrifugation and washed with excess ethanol. The surface of the SERRS nanoparticles was functionalized with (3-mercaptopropyl)trimethoxysilane (MPTMS; 2% (v/v)) in a 90% ethanolic solution (2 hours; 70 ºC) in order to conjugate 2-kDa methoxy-terminated polyethylene glycol (PEG) to the nanoparticle via straightforward maleimide chemistry. The PEGylated SERRS nanoparticles were dispersed in 0.22-μm filter sterilized 10 mM 2-(*N*-morpholino)ethanesulfonic acid (MES) buffer (pH 7.3).

Animal model

All animal experiments were approved by the Institutional Animal Care and Use Committees of Memorial Sloan Kettering Cancer Center (#06-07-011), and all applicable institutional and/or national guidelines for the care and use of animals were followed.

Prostate cancer mouse model (Orthotopic PC-3 model)

A mouse model for prostate cancer metastasis to lymph nodes was generated by orthotopically implanting PC-3 cells (1×10^6 cells in 30 μl 50% matrigel (BD Biosciences) in F-12K medium) stably transduced with a retroviral dual-reporter construct (SFG-click beetle luciferase-IRES-mCherry that was generously provided by Dr. Vladimir Ponomarev) into the left dorsal lobes of the prostates of 8–12 week old C.B-17 severe combined immunodeficiency (SCID, defined flora) male mice ($n = 6$; Taconic, Germantown, NY) [27–28][29]. A cohort of non-tumor-bearing mice ($n = 4$) was included as a control group for this study. Mice were monitored for tumor growth twice a week via bioluminescence imaging (BLI). Briefly, under 2.5% isoflurane anesthesia, tumor-bearing animals were injected retroorbitally with potassium D-luciferin (60 mg/kg) for click beetle luciferase imaging. An IVIS® Spectrum Preclinical In Vivo Imaging System (PerkinElmer, Waltham, MA) was used for bioluminescence signals with an acquisition time of 1 min. Living Image software 2.60 was used to acquire and analyze BLI data.

Optical imaging

Fluorescence and Raman imaging was performed on the same system. A fluorescence microscope (DM2500M, Leica Microsystems Inc., Buffalo Grove, IL) equipped with an ebq 100-04 mercury lamp (Leica Microsystems Inc.), 560 nm excitation and 630 nm emission filters (Chroma 49008 ET-mCh/tR) and a 5× objective (0.12, WD=14 mm; Leica Microsystems Inc.) is integrated in the Renishaw inVia Raman imaging system (Hoffman Estates, IL), with the option to switch between the two imaging modalities. In fluorescence acquisition mode, imaging was recorded with a Lumenera Infinity 3 microscopy camera (Ottawa, Ontario, Canada). The samples were raster-scanned and stitched with Wire 3.4 software (Renishaw Inc., Hoffman Estates, IL). After fluorescence imaging, the inVia imaging system was switched to Raman acquisition mode, and SERRS images of the same samples were acquired using the StreamLine high-speed Raman imaging mode. The inVia Raman system is equipped with a 300-mW 785-nm diode laser and a 1-inch charge-coupled device detector with a spectral resolution of 1.07 cm^{-1} (Renishaw Inc., Hoffman Estates, IL). Raman images were generated from the raw data by applying a direct classical least

square (DCLS) algorithm (Wire 3.4 software, Renishaw), which linearly fits the predefined Raman spectrum of the SERRS nanoparticle to the Raman spectra of the scanned tissues.

Lymph node assessment with Raman imaging and hand-held Raman spectroscopy

At 28 days post implantation, PC-3 prostate cancer-bearing mice ($n = 6$) or control animals ($n = 4$) were injected with 30 fmol/g SERRS nanoparticles intravenously via tail vein. The next day, the animals were euthanized by CO_2 asphyxiation. Exenteration with the removal of the gastrointestinal tract and the pelvic organs, including bladder, prostate, and seminal vesicles, was performed to expose the bilateral medial iliac and subiliac lymph nodes, which were subsequently imaged *in situ* and *ex vivo* by fluorescence (excitation/emission: 560/630 nm) and Raman imaging.

SERRS signal in the lymph nodes *in situ* was also recorded using a hand-held Raman scanner (MiniRam; B&W TEK, Inc., Newark, DE), which is equipped with a 785-nm excitation laser. This system combines a 300-mW 785-nm excitation laser and a thermoelectrically cooled spectrometer in a single unit. This unit is connected to a hand-held probe via excitation- and collection fiberoptics. The spectral range of the system is 175–4000cm^{-1} and resolution 10 cm^{-1}. Scanning was performed by holding the hand-held probe in variable angles, including 90° at a distance of approximately 5 mm from the lymph nodes and with a near real-time acquisition time of 100 ms. Spectral analysis was performed using the B&WSpec 4.01.26 Software (B&W TEK).

Histological analysis

Retroperitoneal tissue and lymph nodes were fixed overnight in 4% paraformaldehyde at 4 °C and subsequently processed for paraffin embedding. Histological analyses on 5-μm tissue sections included hematoxylin-eosin (H&E) and immunohistochemistry staining for human specific Vimentin using the primary antibody from Sigma Aldrich (V6389, 1:5000). A biotin-labeled anti-mouse antibody from Vector Laboratories (BA-9200, 1:300) was used as a secondary antibody. A veterinary pathologist from the Tri-Institutional Laboratory of Comparative Pathology, blinded to the Raman images, examined and graded the H&E and immunohistochemistry slides.

Image- and statistical analysis

Correlation analysis was performed using two different image analysis tools (i.e. using MATLAB v.R2014b (Mathworks, Inc., Natick, MA) and FIJI (with the Coloc2 plugin)). Composite images with and without thresholding (20–50%/maximal intensity) were produced, showing the mCherry fluorescence and the Raman DCLS score. Areas of interest within the LN tissue were selected, the intensities of the two signals therein were compared, and a Pearson coefficient was calculated.

MetaMorph Microscopy Automation and Image Analysis software (Molecular Devices, Sunnyvale, CA) was used to quantify the Raman and fluorescence intensity within the lymph nodes. The MetaMorph protocol used the raw images and separated the Raman and fluorescence images into two different channels and calculated the Raman and fluorescence positive areas, respectively. The mean signal and standard deviations were calculated for the

healthy and infiltrated lymph nodes. A Student's *t*-test (two-tailed, unpaired) was performed and the level of significance was set at $P < 0.05$.

A one-tailed unpaired *t*-test with Welch's correction was used for the analysis of the data for the comparison between the SERRS signal intensities in the medial iliac lymph nodes of healthy control animals versus the PC-3 prostate cancer cell-infiltrated medial iliac lymph nodes. Baseline subtraction was performed using a Whittaker filter with λ=200. Data analysis was performed using MATLAB v.R2014b (Mathworks, Inc., Natick, MA) and PLS Toolbox v.8.0 (Eigenvector Research, Inc., Wenatchee, WA), and statistical analysis with Prism v.6 (Graphpad, Inc., San Diego, CA).

RESULTS

Detection of metastatic lymph nodes in an orthotopic PC-3 prostate cancer mouse model

As shown in Fig. 1b, SERRS nanoparticles used in the current study had a mean diameter of 100 nm with a spectral fingerprint that is uniquely generated by the nanoparticle upon excitation with a 785-nm laser. Upon intravenous injection, the SERRS nanoparticles (30fmol/g) accumulated in organs of the reticuloendothelial system (RES), such as the liver, spleen, and normal lymph nodes (Fig. 1c) in healthy control animals. As shown in Fig. 2, in an established mouse model for prostate cancer metastasis to lymph nodes, we found that infiltration of the medial iliac lymph nodes by PC-3 prostate cancer cells (*i.e.* mCherry fluorescence-positive; Fig. 2b) decreased the accumulation of lymphotropic SERRS nanoparticles (Fig. 2c) following intravenous injection.

Ex vivo Raman imaging of infiltrated and normal lymph nodes

At gross examination, paired bilateral subiliac and medial iliac lymph nodes were harvested. Enlarged medial iliac nodes from both sides with diameters of ~1 mm were observed compared to the subiliac nodes with diameters of ~600 μm. Interestingly, complementary images obtained by *ex vivo* fluorescence and Raman imaging showed high fluorescence and low SERRS signal in the medial iliac nodes, while low fluorescence and high SERRS signal was detected in normal subiliac nodes (Fig. 3a). Immunohistochemistry staining further confirmed the presence of human prostate cancer cells (human Vimentin^{+}) only in SERRS nanoparticle-negative areas of the medial lymph nodes (Fig. 3b). These data demonstrate that the prostate cancer cells, which invade into lymph nodes, decrease the uptake of SERRS nanoparticles in the respective areas of the lymph node. Quantitative assessment of the Raman- and fluorescence-signal intensities of each imaged lymph node was performed and it was found that the distribution of the SERRS nanoparticle signal correlated inversely with the fluorescence intensity in the lymph nodes (Pearson coefficient $\rho = -0.55$ without thresholding; $\rho = <-0.7$ with 30% thresholding), indicating that the prostate cancer metastasis within the medial iliac lymph nodes (red) replaced the healthy, macrophage-rich lymph node tissue outlined by the SERRS nanoprobes (green). The mean ± SD of SERRS- or fluorescence positive areas (%) within each lymph node were determined and plotted for both the normal and infiltrated lymph nodes. As shown in Fig. 3c, the SERRS signal decreased significantly when the lymph node was infiltrated by metastatic prostate cancer cells.

Since in a clinical setting a diagnosis would be made solely based on the SERRS signal intensity and appearance, we compared the SERRS signal intensities of the lymph nodes infiltrated with prostate cancer with lymph nodes of healthy control animals and found a significant (p=0.0057) difference in SERRS signal intensities between both groups (Fig. 4)

Detection of lymph node infiltration with a hand-held Raman spectrometer

To demonstrate the potential application of a hand-held Raman spectrometer as a tool for intraoperative detection of lymph node infiltration during radical prostatectomy, we performed Raman scanning of the bilateral medial iliac and subiliac lymph nodes in the orthotopic PC-3 prostate cancer mouse model using a 785-nm excitation laser MiniRam Raman hand-held scanner (n = 4). As a result of the high sensitivity of the SERRS nanoparticles, with a limit of detection in the low femtomolar range, (near-) real time acquisition times (100 ms) could be used to scan the aforementioned lymph nodes. The unique Raman spectrum of SERRS nanoparticles excited with the 785-nm laser was detected in the subiliac lymph nodes, while no SERRS nanoparticles were detected by hand-held Raman surveillance in the medial iliac lymph nodes (Fig. 5) providing immediate indication that the medial iliac lymph nodes were infiltrated by PC-3 prostate cancer cells, which was confirmed by immunohistochemistry (Fig. 3b).

DISCUSSION

In this study, we report the ability of our recently developed SERRS nanoparticles to discriminate between healthy and metastatic lymph nodes in an orthotopic PC-3 prostate cancer mouse model, which was corroborated by immunohistochemistry and, as a second independent modality, by the mCherry-fluorescence of the tumor cells. The size of the lymph nodes in the PC-3 mouse model ranged between 0.7 – 1.5 mm in short axis. These dimensions are approximately 10-fold smaller than those in humans, providing a glimpse into the superiority of the SERRS nanoparticle technology over currently available imaging methods. Aside from using a Raman imaging instrument to acquire whole Raman maps, we also found that lymph nodes could be probed in real-time with a hand-held Raman scanner that is commercially available. This hand-held scanner has already been used in clinical trials using intrinsic Raman spectroscopy in other cancer types [30–31].

Prior studies reported the mechanism of accumulation of SPIONs [32] in animal and human lymph nodes after extravasation from the vascular into the interstitial space, transport via the lymphatic vessels, and internalization by macrophages [19, 33–34]. Harisinghani *et al.* investigated the use of SPIONs as a MRI contrast agent for the detection of lymph node metastases in 80 patients with clinical stage T1, T2, or T3 prostate cancer who underwent surgical resection or biopsy of pelvic lymph nodes [20]. Nodal metastases altered the nodal architecture allowing MRI to detect abnormal patterns of nanoparticle accumulation. Sensitivity of MRI with lymphotropic superparamagnetic nanoparticles was 100% in patients with nodal metastases and 96% in lymph node metastasis-free patients. Positive and negative predictive values significantly increased from 60% and 67%, respectively, for MRI alone to 94% and 100%, respectively, for MRI with lymphotropic superparamagnetic nanoparticles.

Despite the major differences in size and surface chemistry, our study showed that the SERRS nanoparticles behaved very similar to the well-established SPIONs. However, there are major differences between the two detection methods. MRI generally can provide a *pre*- but not an *intra*-operative assessment of the lymph node status. The SERRS nanoparticle approach could allow surgeons to assess individual lymph nodes intraoperatively in a time-efficient and sensitive manner with spatial resolution far superior than MRI.

The ability of SERRS NPs to detect partial metastatic infiltration of lymph nodes is important because such micro-metastases typically do not result in an increase in lymph node size detectable with conventional imaging methods such as MRI or CT. In addition, as shown by Cheng *et al.*, partial lymph node metastases are very common: In their study, 28% of patients had less than 25%, 45% less than 45%, and 65% less than 90% cancerous lymph node replacement [35].

Rapid wide-field Raman imaging devices for clinical use are currently not yet available, however, their development is underway [36]. Raman hand-held scanners, on the other hand, are already commercially available. We therefore demonstrated the potential application of a hand-held Raman scanner that can be used to rapidly probe each lymph node in question, and could be used as an alternative detection device until wide-field Raman scanners are available. Due to the low femtomolar or even attomolar [37] limits of detection of the SERRS nanoparticles, very short acquisition times (100 ms) can be used enabling near real-time surveillance. Furthermore, since the spectral fingerprint is unique to the SERRS nanoparticle, we are currently developing software that upon detection of the SERRS nanoparticles' spectral fingerprint triggers an acoustic signal that, depending on the intensity of the signal, will change its pitch.

With clinical translation in mind, the SERRS nanoparticles are synthesized without the use of toxic substances and consist of inert materials. SERS nanoparticles of similar size, materials, and surface composition have already passed extensive cytotoxicity studies [38] and therapeutic gold or gold-silica nanoparticles are in advanced clinical trials [39]. While in general gaining FDA-approval of nanoparticle imaging agents is more challenging than small molecule agents, we do believe that these precedents and the particles' biocompatibility will result in a high chance for successful clinical translation. To this end, it is noteworthy that we have recently generated a newer generation of SERRS nanoparticles, which have an order-of-magnitude lower limit of detection (*i.e.* 100 attomolar) than the ones used in the current study [37]. Due to this higher sensitivity, the new generation of SERRS nanoparticles could enable the determination of lymph node status with a fraction of the dose that was needed for the SERRS nanoparticles applied in current study.

In summary, the SERRS nanoparticles approach presented here has the potential to allow real-time determination of the status – healthy vs. tumor-invaded – of lymph nodes. Because the SERRS principle interrogates lymph nodes directly, it represents a major advance over sentinel lymph node imaging methods. Sentinel lymph node techniques can only identify the first draining lymph node, but do not inform about its status, or the status of any other lymph node upstream. Therefore, with sentinel lymph node techniques it remains unknown whether or not any lymph node contains cancer until pathological examination has been performed.

The mechanism with which the SERRS nanoparticles detect metastases does not rely on the expression of a specific cancer marker, but instead a biological phenomenon common to all cancer types. Thus, SERRS nanoparticles are in principle not limited to prostate cancer presented herein, but in fact are likely to perform similarly in most other cancer types.

SERRS nanoparticles might ultimately enable rapid intraoperative diagnosis and selective dissection of only those lymph nodes that are metastasized. This could result in reduced operating times; decreased morbidity, complications; and costs; and improved clinical and oncological outcomes compared to patients undergoing extensive lymph node resections for cancer.

Acknowledgments

The authors would like to thank Vladimir Ponomarev, PhD (MSKCC) for providing SFG-click beetle luciferase-IRES-mCherry cells; the Electron Microscopy and Molecular Cytology Core Facility at MSKCC; Julie White, PhD from the Tri-Institutional Laboratory of Comparative Pathology for interpreting the histological results; Matthew B. Brendel from the Molecular Cytology Core Facility at MSKCC for providing assistance with image analysis and quantification; and Andrew Cho and Marc Levine (Kircher lab, MSKCC) for critical review of the manuscript. **Funding:** NIH R01 EB017748 (M.F.K.); NIH K08 CA16396 (M.F.K.); M.F.K. is a Damon Runyon-Rachleff Innovator supported (in part) by the Damon Runyon Cancer Research Foundation (DRR-29–14); Pershing Square Sohn Prize by the Pershing Square Sohn Cancer Research Alliance (M.F.K.). MSKCC Center for Molecular Imaging and Nanotechnology (CMINT) Grant, Technology Development Grant, Experimental Therapeutics Grant and Molecularly Targeted Intra-Operative Imaging Grant (M.F.K.); Geoffrey Beene Cancer Research Center at MSKCC Grant Award and Shared Resources Award (M.F.K.); Bayer HealthCare Pharmaceuticals/RSNA Research Scholar Grant (M.F.K.). M.S. received salary support by the Department of Surgery of MSKCC (Chair: P.T.S). M.A.W. was supported by a National Science Foundation Integrative Graduate Education and Research Traineeship Grant (NSF, IGERT 0965983 at Hunter College). This research was funded in part through the NIH/NCI Cancer Center Support Grant P30 CA008748.

References

1. Siegel RL, Miller KD, Jemal A. Cancer statistics, 2015. CA Cancer J Clin. 2015; 65:5–29. [PubMed: 25559415]
2. Yossepowitch O, Eggener SE, Serio AM, et al. Secondary therapy, metastatic progression, and cancer-specific mortality in men with clinically high-risk prostate cancer treated with radical prostatectomy. Eur Urol. 2008; 53:950–959. [PubMed: 17950521]
3. Allaf ME, Palapattu GS, Trock BJ, Carter HB, Walsh PC. Anatomical extent of lymph node dissection: impact on men with clinically localized prostate cancer. J Urol. 2004; 172:1840–1844. [PubMed: 15540734]
4. Bader P, Burkhard FC, Markwalder R, Studer UE. Is a limited lymph node dissection an adequate staging procedure for prostate cancer? J Urol. 2002; 168:514–518. discussion 518. [PubMed: 12131300]
5. Godoy G, von Bodman C, Chade DC, et al. Pelvic lymph node dissection for prostate cancer: frequency and distribution of nodal metastases in a contemporary radical prostatectomy series. J Urol. 2012; 187:2082–2086. [PubMed: 22498221]
6. Heidenreich A, Varga Z, Von Knobloch R. Extended pelvic lymphadenectomy in patients undergoing radical prostatectomy: high incidence of lymph node metastasis. J Urol. 2002; 167:1681–1686. [PubMed: 11912387]
7. von Bodman C, Godoy G, Chade DC, et al. Predicting biochemical recurrence-free survival for patients with positive pelvic lymph nodes at radical prostatectomy. J Urol. 2010; 184:143–148. [PubMed: 20478587]
8. Bader P, Burkhard FC, Markwalder R, Studer UE. Disease progression and survival of patients with positive lymph nodes after radical prostatectomy. Is there a chance of cure? J Urol. 2003; 169:849–854. [PubMed: 12576797]

9. Godoy G, Chong KT, Cronin A, et al. Extent of pelvic lymph node dissection and the impact of standard template dissection on nomogram prediction of lymph node involvement. Eur Urol. 2011; 60:195–201. [PubMed: 21257258]
10. Feifer AH, Elkin EB, Lowrance WT, et al. Temporal trends and predictors of pelvic lymph node dissection in open or minimally invasive radical prostatectomy. Cancer. 2011; 117:3933–3942. [PubMed: 21412757]
11. Kawakami J, Meng MV, Sadetsky N, et al. Changing patterns of pelvic lymphadenectomy for prostate cancer: results from CaPSURE. J Urol. 2006; 176:1382–1386. [PubMed: 16952638]
12. Abdollah F, Sun M, Thuret R, et al. Decreasing rate and extent of lymph node staging in patients undergoing radical prostatectomy may undermine the rate of diagnosis of lymph node metastases in prostate cancer. Eur Urol. 2010; 58:882–892. [PubMed: 20932637]
13. Silberstein, JL.; Laudone, VP. Pelvic Lymph Node Dissection. In: Eastham, JA.; Schaeffer, EM., editors. Radical Prostatectomy. New York, NY: Springer; 2015. p. 57-74.
14. Cagiannos I, Karakiewicz P, Eastham JA, et al. A preoperative nomogram identifying decreased risk of positive pelvic lymph nodes in patients with prostate cancer. J Urol. 2003; 170:1798–1803. [PubMed: 14532779]
15. Abdollah F, Sun M, Suardi N, et al. National Comprehensive Cancer Network practice guidelines 2011: Need for more accurate recommendations for pelvic lymph node dissection in prostate cancer. J Urol. 2012; 188:423–428. [PubMed: 22698627]
16. Nepple KG, Rosevear HM, Stolpen AH, Brown JA, Williams RD. Concordance of preoperative prostate endorectal MRI with subsequent prostatectomy specimen in high-risk prostate cancer patients. Urol Oncol. 2013; 31:601–606. [PubMed: 21665495]
17. Meinhardt W, Valdes Olmos RA, van der Poel HG, Bex A, Horenblas S. Laparoscopic sentinel node dissection for prostate carcinoma: technical and anatomical observations. BJU Int. 2008; 102:714–717. [PubMed: 18410427]
18. van der Poel HG, Buckle T, Brouwer OR, Valdes Olmos RA, van Leeuwen FW. Intraoperative laparoscopic fluorescence guidance to the sentinel lymph node in prostate cancer patients: clinical proof of concept of an integrated functional imaging approach using a multimodal tracer. Eur Urol. 2011; 60:826–833. [PubMed: 21458154]
19. Weissleder R, Elizondo G, Wittenberg J, Lee AS, Josephson L, Brady TJ. Ultrasmall superparamagnetic iron oxide: an intravenous contrast agent for assessing lymph nodes with MR imaging. Radiology. 1990; 175:494–498. [PubMed: 2326475]
20. Harisinghani MG, Barentsz J, Hahn PF, et al. Noninvasive detection of clinically occult lymph-node metastases in prostate cancer. N Engl J Med. 2003; 348:2491–2499. [PubMed: 12815134]
21. Kircher MF, Willmann JK. Molecular body imaging: MR imaging, CT, and US. part I. principles. Radiology. 2012; 263:633–643. [PubMed: 22623690]
22. Kircher MF, Willmann JK. Molecular body imaging: MR imaging, CT, and US. Part II. Applications. Radiology. 2012; 264:349–368. [PubMed: 22821695]
23. Andreou C, Kishore SA, Kircher MF. Surface-Enhanced Raman Spectroscopy: A New Modality for Cancer Imaging. Journal of nuclear medicine : official publication, Society of Nuclear Medicine. 2015; 56:1295–1299.
24. Kircher MF, de la Zerda A, Jokerst JV, et al. A brain tumor molecular imaging strategy using a new triple-modality MRI-photoacoustic-Raman nanoparticle. Nat Med. 2012; 18:829–834. [PubMed: 22504484]
25. Karabeber H, Huang R, Iacono P, et al. Guiding brain tumor resection using surface-enhanced Raman scattering nanoparticles and a hand-held Raman scanner. ACS Nano. 2014; 8:9755–9766. [PubMed: 25093240]
26. Harmsen S, Huang R, Wall MA, et al. Surface-enhanced resonance Raman scattering nanostars for high-precision cancer imaging. Sci Transl Med. 2015; 7:271ra277.
27. Kaighn ME, Narayan KS, Ohnuki Y, Lechner JF, Jones LW. Establishment and characterization of a human prostatic carcinoma cell line (PC-3). Invest Urol. 1979; 17:16–23. [PubMed: 447482]
28. Sobel RE, Sadar MD. Cell lines used in prostate cancer research: a compendium of old and new lines--part 1. J Urol. 2005; 173:342–359. [PubMed: 15643172]

29. Huang R, Vider J, Serganova I, Blasberg RG. ATP-binding cassette transporters modulate both coelenterazine- and D-luciferin-based bioluminescence imaging. Mol Imaging. 2011; 10:215–226. [PubMed: 21496450]

30. Horsnell J, Stonelake P, Christie-Brown J, et al. Raman spectroscopy--a new method for the intra-operative assessment of axillary lymph nodes. Analyst. 2010; 135:3042–3047. [PubMed: 21046027]

31. Horsnell JD, Smith JA, Sattlecker M, et al. Raman spectroscopy--a potential new method for the intra-operative assessment of axillary lymph nodes. Surgeon. 2012; 10:123–127. [PubMed: 22525413]

32. Grimm J, Kircher MF, Weissleder R. Cell tracking : Principles and applications. Der Radiologe. 2007; 47:25–33. [PubMed: 17187264]

33. Harisinghani MG, Saini S, Weissleder R, et al. MR lymphangiography using ultrasmall superparamagnetic iron oxide in patients with primary abdominal and pelvic malignancies: radiographic-pathologic correlation. AJR Am J Roentgenol. 1999; 172:1347–1351. [PubMed: 10227514]

34. Wunderbaldinger P, Josephson L, Bremer C, Moore A, Weissleder R. Detection of lymph node metastases by contrast-enhanced MRI in an experimental model. Magn Reson Med. 2002; 47:292–297. [PubMed: 11810672]

35. Cheng L, Bergstralh EJ, Cheville JC, et al. Cancer volume of lymph node metastasis predicts progression in prostate cancer. Am J Surg Pathol. 1998; 22:1491–1500. [PubMed: 9850175]

36. Andreou C, Kishore SA, Kircher MF. Surface-Enhanced Raman Spectroscopy: A New Modality for Cancer Imaging. J Nucl Med. 2015 Jul 16. [Epub ahead of print].

37. Harmsen S, Bedics MA, Wall MA, Huang R, Detty MR, Kircher MF. Rational design of a chalcogenopyrylium-based surface-enhanced resonance Raman scattering nanoprobe with attomolar sensitivity. Nat Commun. 2015; 6:6570. [PubMed: 25800697]

38. Thakor AS, Luong R, Paulmurugan R, et al. The fate and toxicity of Raman-active silica-gold nanoparticles in mice. Science translational medicine. 2011; 3:79ra33.

39. Thakor AS, Gambhir SS. Nanooncology: the future of cancer diagnosis and therapy. CA Cancer J Clin. 2013; 63:395–418. [PubMed: 24114523]

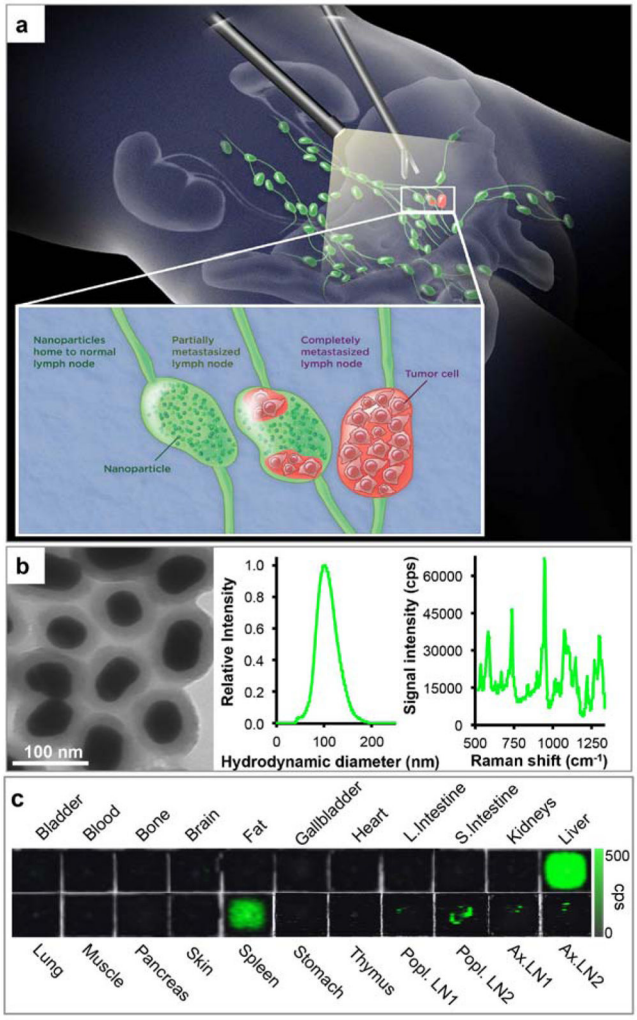

Figure 1. SERRS-based Raman imaging for the detection of prostate cancer lymph node metastases

a. Concept. SERRS nanoparticles are injected intravenously, reach lymph nodes via interstitial-lymphatic fluid transport and internalize into macrophages within healthy lymph nodes. Magnified inset: In normal lymph nodes (left) the nanoparticles are taken up avidly by resident macrophages. If a lymph node is either partially (middle) or completely (right) invaded by metastatic prostate cancer cells, the resident macrophages are replaced by tumor tissue, resulting in a marked decrease in nanoparticle uptake. **b.** Transmission electron micrograph (left), nanoparticle size distribution determined with nanoparticle tracking analysis (middle), and Raman spectrum of the SERRS nanoparticles upon excitation with a 785-nm laser (right). **c.** Tissue distribution of the SERRS nanoparticles in a representative healthy mouse. Raman signal of the 950 cm^{-1} in counts per second.

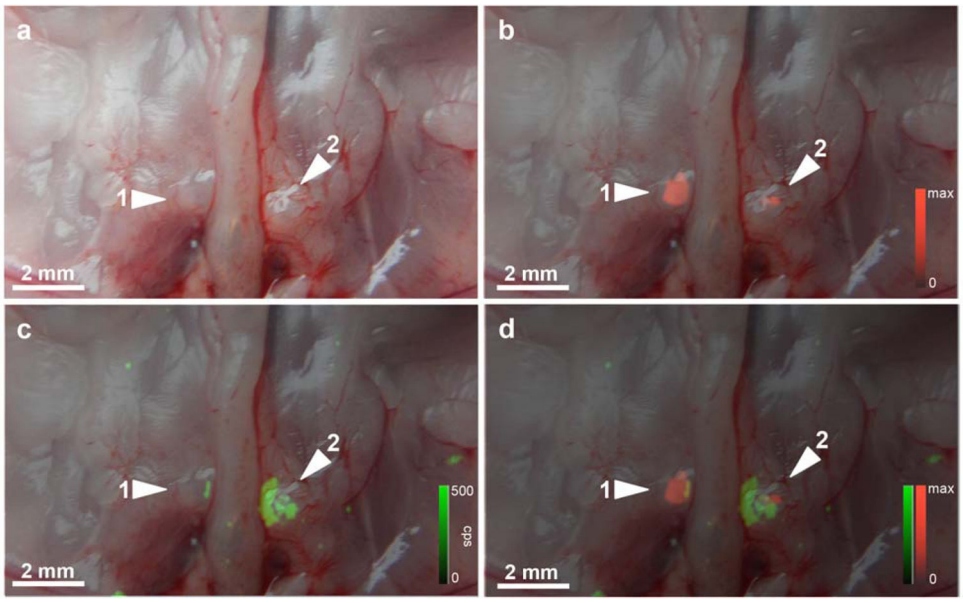

Figure 2. ***In situ*** **fluorescence and Raman imaging of lymph node metastases in an orthotopic mCherry-transduced PC-3 prostate cancer mouse model**

Animals were injected 16–18 h prior i.v. with SERRS nanoparticles. a. Photograph of the retroperitoneum after radical prostatectomy. Medial iliac lymph nodes are indicated by arrowheads. b. Fluorescence/white-light overlay of the retroperitoneum shows the fluorescence signal of mCherry-transduced PC-3 cells (red pseudocolor) in the medial iliac lymph nodes, indicating the presence of lymph node metastases. c. Raman (green pseudocolor)/white-light overlay and d. Raman/mCherry-fluorescence/white-light overlay of the same lymph nodes shows SERRS signal only in those areas of the lymph nodes that are not replaced by tumor cells.

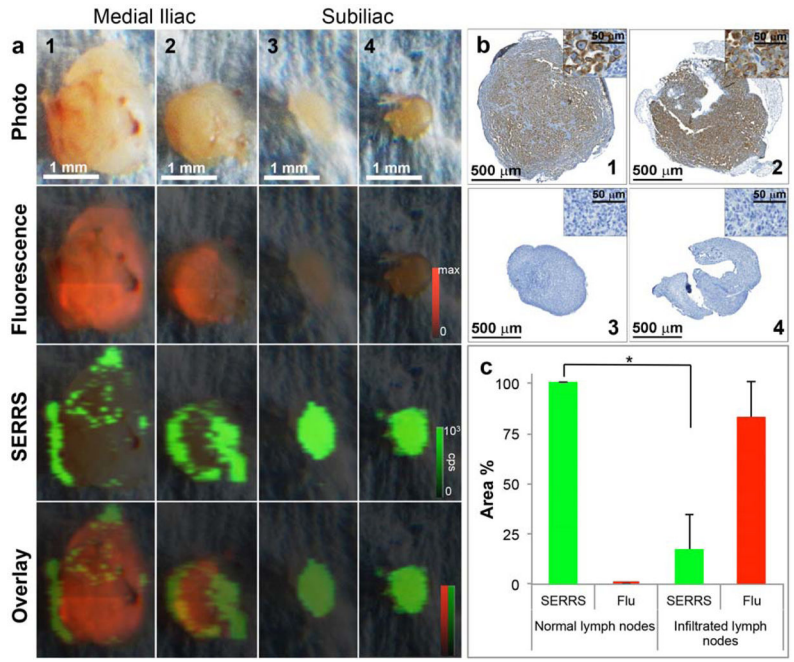

Figure 3. ***Ex vivo*** **imaging of medial and subiliac lymph nodes in the orthotopic mCherry-transduced PC-3 prostate cancer mouse model in a different animal**

a. Photograph of medial iliac (1–2) and subiliac lymph nodes (3–4). Fluorescence imaging (mCherry-transduced PC-3 cells) demonstrates mCherry signal almost throughout both medial iliac lymph nodes, indicating near complete metastatic replacement. In contrast, no fluorescence was detected in the subiliac lymph nodes, indicating a lack of infiltration of PC-3 in these lymph nodes. While Raman imaging showed homogenous SERRS signal due to avid uptake of the SERRS nanoparticles in the normal subiliac lymph nodes, hypointense SERRS regions (green) were detected within the medial iliac lymph nodes, which is consistent with displacement of normal lymph node architecture by malignant infiltration. b. Immunohistochemical staining of the lymph nodes with the anti-human Vimentin antibody (selective staining for PC-3 cells) corroborated that the mCherry fluorescence in the medial iliac lymph nodes correlated with the tumor burden. Note that the mCherry-low areas in the diseased nodes match closely with SERRS positive areas. c. Quantitative assessment of Raman signal intensity in normal versus infiltrated lymph nodes. The mean Raman and fluorescence (Flu) areas (%) were obtained by determining the Raman (green)- and/or fluorescence (red) positive areas within a lymph node. Healthy lymph nodes demonstrated ~100% Raman signal intensity, which significantly decreased when the lymph node was infiltrated by PC-3 cells ($p < 0.05$). The signal intensity is expressed as mean ± SD.

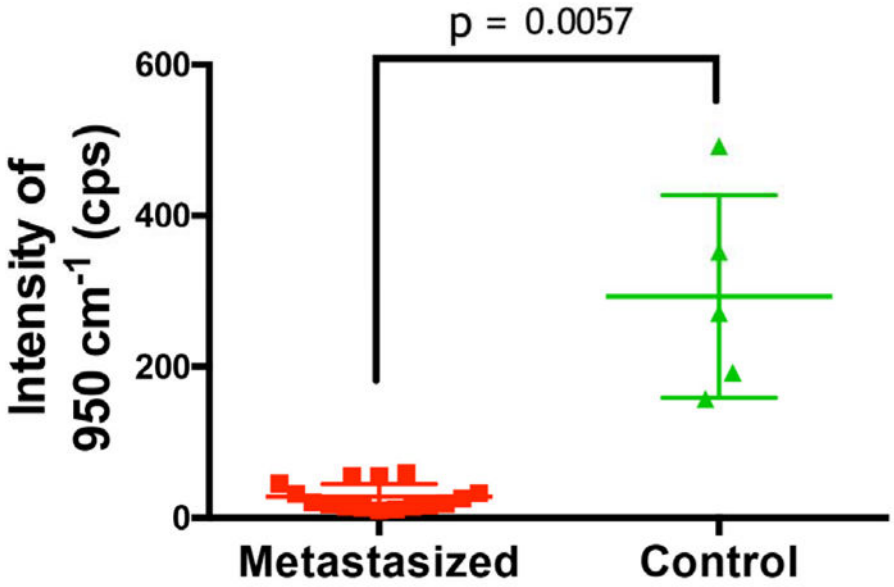

Figure 4. SERRS signal intensity comparison between nodes of healthy control animals versus PC-3 cell-infiltrated nodes

Lymph nodes were identified in healthy control and prostate cancer bearing animals. For each the average intensity of the 950 cm^{-1} band after baseline subtraction was recorded. Metastasized lymph nodes showed distinctly lower Raman signal than healthy controls, which was statistically significant with a *p*-value of 0.0057.

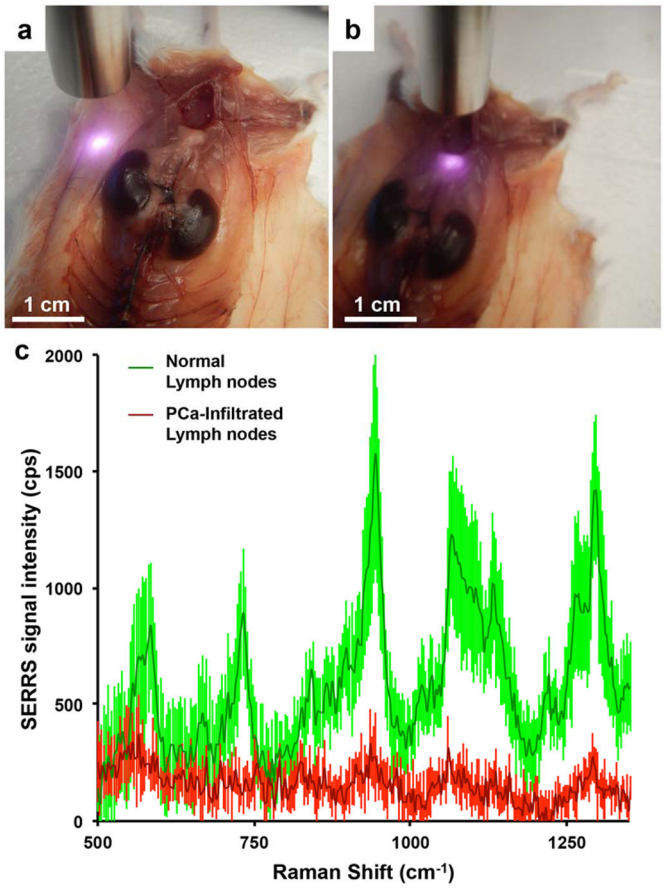

Figure 5. Feasibility of detecting lymph node metastases with a hand-held Raman spectroscopy scanner in near real-time

In situ hand-held Raman scanning (785 nm, 10-mW laser power, 100-ms acquisition time) was performed on **a.** healthy subiliac lymph nodes and, **b.** metastasized medial iliac lymph nodes. **c.** While the Raman fingerprint of the SERRS nanoparticles is detected in the healthy lymph nodes (green spectrum), a significant ($p < 0.05$) decrease in SERRS signal of the 950 cm^{-1} peak was found in the diseased lymph nodes (red). Data represent at least four different experiments and are presented as mean normalized SERRS spectra±SD.